Virtual bremsstrahlung in proton-proton scattering below the pion-production threshold

J. G. Messchendorp,* J. C. S. Bacelar, M. J. van Goethem, M. N. Harakeh, M. Hoefman, H. Huisman,
N. Kalantar-Nayestanaki, H. Löhner, R. W. Ostendorf, S. Schadmand,* R. Turrisi,† M. Volkerts, and H. W. Wilschut

Kernfysisch Versneller Instituut, Zernikelaan 25, NL-9747 AA Groningen, The Netherlands

R. S. Simon

Gesellschaft für Schwerionenforschung, Planckstraße 1, D-64291 Darmstadt, Germany

Exclusive differential cross sections of virtual bremsstrahlung in proton-proton scattering below the pion-production threshold have been measured and their leptonic-angle dependence was exploited to determine all six nucleon-nucleon electromagnetic response functions in the timelike region. The data are compared to a low-energy calculation and a fully relativistic microscopic model. Over the entire phase space the low-energy calculation gives a better description of the cross sections than does the microscopic model. At large virtual-photon masses both models are unable to account for the observed strength of the interference response functions.

I. INTRODUCTION

A detailed knowledge of the interaction between nucleons is essential for the understanding of nuclear phenomena. It is therefore of great interest to have a good description of the NN interaction. To this end, experimental and theoretical studies of the system in which two nucleons interact are of importance. This has led to extensive studies of the elastic pp and pn scattering processes. Cross sections and spin observables are experimentally well determined, and are well described by present models [1–3]. The available data are used to fit parameters of the nucleon-nucleon interaction potential, which include higher-order effects, such as off-shell contributions. A process which is potentially sensitive to off-shell effects is the inelastic scattering of two nucleons with the emission of a photon (NN bremsstrahlung). In this process, as illustrated in Fig. 1, already at the lowest-order contribution in V, the nucleon is off the mass shell due to the presence of the photon. The availability of high-luminosity, polarized proton beams has recently opened up the possibility of experimental studies of the bremsstrahlung process which have provided cross sections and analyzing powers with outstanding accuracies [4–6].

Closely related to the bremsstrahlung process $pp \rightarrow pp\gamma$ is the so-called virtual-bremsstrahlung reaction $pp \rightarrow ppe^+e^-$. This process involves the production of a lepton pair (e^+e^-), which, according to the theory of quantum electrodynamics (QED), can be described by the emission of a virtual photon. By studying virtual-photon production, new features can be added to the information already obtained from the real-photon process. First of all, a virtual photon can be longitudinally polarized, in contrast with a real photon, and is able therefore to probe electromagnetic currents which propagate in the direction of the photon. Secondly,

from the angular distribution of the two leptons, the reaction cross section can be decomposed into six different components. Each of these components is related to a specific polarization state of the virtual photon. This gives additional observables (response functions) which are sensitive to specific ingredients of the reaction mechanism (i.e., negative-energy states, Δ resonances, meson-exchange contributions, etc.) [7]. Virtual bremsstrahlung, therefore, allows a detailed analysis of the pp interaction.

Experimentally, measuring the $pp \rightarrow ppe^+e^-$ reaction process is far from easy. The cross section is approximately a factor $\alpha = 1/137$ smaller than the real-photon process. Integrated over 4π and the virtual-photon mass the cross section is ≈ 10 nb, as predicted by a low-energy calculation. Thus, in order to measure virtual bremsstrahlung, a high integrated luminosity together with an efficient detector system subtending a large solid angle is required.

So far, e^+e^- production in proton-proton scattering has been studied only at an incident beam energy of 4.9 GeV [8,9]. This high-energy experiment was performed with the DiLepton Spectrometer (DLS) [10] at the Bevalac and deter-
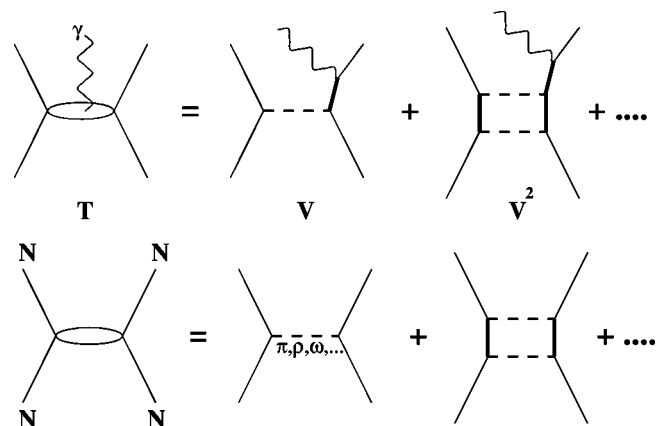

FIG. 1. Leading-order diagrams needed for the calculation of the $p+p$ elastic amplitude (bottom) and the real- and virtual-bremsstrahlung amplitudes (top). V and T are the nucleon-nucleon potential and the T matrix, respectively.

---

*Present address: Universität Gießen, Heinrich-Buff-Ring 16, D-35392 Gießen, Germany.

†Present address: Dipartimento di Fisica dell'Università, Corso Italia 57, I-95129 Catania, Italy.

mined the mass and transverse-momentum dependence of the dilepton yield. At 4.9 GeV the dileptons originate mainly from mesonic decays and the contribution from bremsstrahlung is small. The present experiment follows a different approach. It measures $pp \rightarrow ppe^+e^-$ at a proton energy of 190 MeV, well below the meson-production thresholds. At this energy bremsstrahlung is the only source of dileptons.

The experiment has been performed with the superconducting-cyclotron AGOR of the Kernfysisch Versneller Instituut (KVI) in Groningen. All four reaction products (two protons and two leptons) were measured by a coincidence setup featuring the small-angle large-acceptance detector (SALAD) [11] and the two-arm photon spectrometer (TAPS) [12]. A total of 600 events were identified with the $pp \rightarrow ppe^+e^-$ process.

The outline of this paper is as follows. First, we introduce the observables which characterize the virtual-bremsstrahlung process, followed by a short description of the models used to interpret the data. Next, the experimental procedure for the measurement of the $pp \rightarrow ppe^+e^-$ reaction is outlined. Subsequently, the analysis of the data is discussed, including the data reduction procedure, the background study, the normalization of the data to obtain differential cross sections, and the extraction of the response functions. Finally, the experimental results are compared with theoretical predictions. A brief description of this experiment and its results has been reported in Refs. [13–16].

II. CROSS SECTIONS AND RESPONSE FUNCTIONS

Triggered by the experimental development, substantial progress has been achieved in refining the theoretical models that describe the $pp \rightarrow ppe^+e^-$ reaction. In this paper, we compare the experimental cross sections and electromagnetic response functions to predictions based on a relativistic low-energy theorem [17,18], as well as to the predictions of a fully relativistic microscopic calculation by Martinus *et al.* [7].

The differential cross section of the $pp \rightarrow ppe^+e^-$ process can be written as [17,18]

$$\frac{d^8\sigma}{d\Omega_{p_1}d\Omega_{p_2}dM_\gamma d\theta_\gamma d\cos\theta_l d\phi_l} = \frac{m_p^4 m_l^2}{(2\pi)^8 F}|A|^2 R, \quad (1)$$

where p_1 and p_2 are the outgoing protons, M_γ is the virtual-photon mass, θ_γ its polar angle, θ_l and ϕ_l are the leptonic energy-sharing angle and dihedral angle, respectively (see Fig. 2). In the laboratory system with the target proton at rest the flux factor F is given as $F = m_p|\vec{p}|$. Here $\vec{p}$ is the three-momentum of the incoming proton and m_p is the proton rest mass. The term $|A|^2$ is the square of the invariant amplitude of the virtual-photon production $pp \rightarrow ppe^+e^-$. The Lorentz-invariant phase-space factor, R, is given by

$$R = \frac{4|\vec{l}|^3}{M_\gamma(1 - 4m_l^2/M_\gamma^2)k_0}\delta^4(p - p_1 - p_2 - k), \quad (2)$$
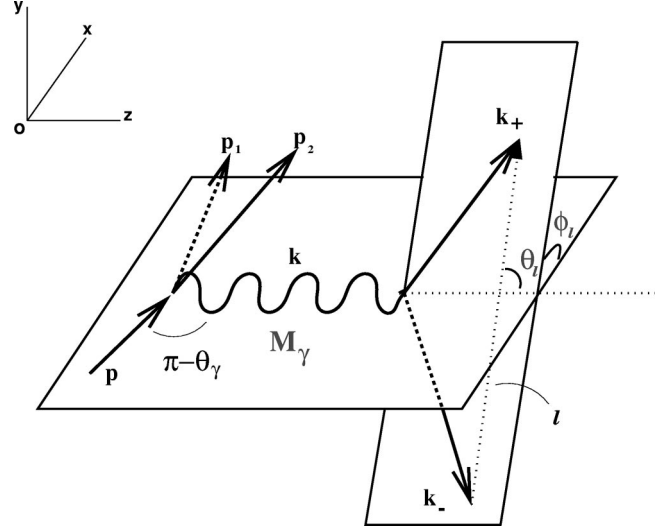

FIG. 2. Schematic diagram of the coordinate system (lab frame) used for the definition of the response functions for the $pp \rightarrow ppe^+e^-$ reaction.

$$\frac{p_1^2 dp_1 p_2^2 dp_2 k^2 dk}{E_{p_1}E_{p_2}k_0}\sin\theta_\gamma d\phi_\gamma.$$

The four-momenta $\vec{l} = (k_+ - k_-)$ and $k = (k_+ + k_-)$, where the four-momenta $k_+ = (E_+, \vec{k}_+)$ and $k_- = (E_-, \vec{k}_-)$ refer to the leptons (positron and electron) with mass m_l. The transition amplitude A can be obtained by coupling the nucleonic current, represented by J, to the leptonic current, represented by j. This coupling is described by QED. The square of the amplitude is given by

$$|A|^2 = \frac{e^4}{M_\gamma^4}|j^\mu J_\mu|^2 = -\frac{e^4}{2m_l^2 M_\gamma^4}[|J\cdot l|^2 + M_\gamma^2(J\cdot J^*)], \quad (3)$$

where we have dropped the indices for J. From expression (3) one clearly sees that $|A|^2$ is a sum of quadratic terms of the hadronic current J.

The aim now is to express the cross section for $pp \rightarrow ppe^+e^-$, analogously to the longitudinal-transverse decomposition for electron-scattering processes [19,20], in terms of a set of independent *electromagnetic response functions*. The spatial part of the current J is decomposed into a longitudinal (parallel to the virtual-photon direction) and a transverse component (perpendicular to the virtual-photon direction). Furthermore, the latter can be decomposed into two orthogonal contributions, a left- and a right-handed circularly polarized component. Details can be found in the Appendix.

A convenient coordinate system in which to define the projection of the current J_μ is depicted in Fig. 2. Here, the photon momentum is chosen along the axis OZ and XOZ is taken as the plane of the incoming proton and virtual photon (reaction plane). As a result, the momentum of the incoming proton (in the lab frame), $\vec{p}$, has the components $(p_x, 0, p_z)$. In this coordinate system one defines the six electromagnetic response functions: W_T (transverse), W_L (longitudinal), W_{TT}

TABLE I. Nucleon response functions W_i and the factors C_i determining the $pp \to ppe^+e^-$ cross section. $J_{x,y,z}$ are the covariant nucleonic currents, for the coordinate system depicted in Fig. 2. W_T and W_L are the transverse and longitudinal nucleon response functions. W_{TT}, W'_{TT}, W_{LT}, and W'_{LT} are the interference terms.

Term	W	C
W_T	$J_x J_x^* + J_y J_y^*$	$\left(1 - \dfrac{(\vec{l})^2}{2M_\gamma^2} \sin^2 \theta_l\right)$
W_L	$\dfrac{M_\gamma^2}{k_0^2} \lvert J_z \rvert^2$	$\left(1 - \dfrac{(\vec{l})^2}{k_0^2} \cos^2 \theta_l\right)$
W_{TT}	$J_y J_y^* - J_x J_x^*$	$\left.\begin{array}{c}\ \\ \ \end{array}\right\} \dfrac{(\vec{l})^2 \sin^2 \theta_l}{2M_\gamma^2}$
W'_{TT}	$-2 \, \mathrm{Re}(J_x J_y^*)$	
W_{LT}	$-2 \dfrac{M_\gamma}{k_0} \mathrm{Re}(J_z J_x^*)$	$\left.\begin{array}{c}\ \\ \ \end{array}\right\} \dfrac{(\vec{l})^2 \sin 2\theta_l}{2k_0 M_\gamma}$
W'_{LT}	$-2 \dfrac{M_\gamma}{k_0} \mathrm{Re}(J_z J_y^*)$	

(transverse-transverse), W_{LT} (longitudinal-transverse), W'_{TT} (transverse-transverse prime), W'_{LT} (longitudinal-transverse prime), as given in the left column of Table I (see the Appendix for details). Equation (3) takes the following form when expressed in terms of these response functions:

$$|A|^2 = \frac{e^4}{2m_l^2 M_\gamma^2} \{ W_T C_T + W_L C_L + C_{TT}(W_{TT} \cos 2\phi_l + W'_{TT} \sin 2\phi_l) + C_{LT}(W_{LT} \cos \phi_l + W'_{LT} \sin \phi_l) \}, \quad (4)$$

where the factors C_i are defined in the right column of Table I. The derivation of this decomposition is given in the Appendix. The angles θ_l and ϕ_l in Eq. (4) are the polar and the azimuthal angle of the vector $\vec{l}$ in the lab system, respectively, as schematically drawn in Fig. 2.

Equation (4) shows how to extract the different response functions, W_i, experimentally. This can be achieved by determining the dependence of the differential cross section on the leptonic angles (θ_l, ϕ_l), and making use of the orthogonality of the trigonometric functions $\cos n\phi_l$ and $\sin n\phi_l$. In order to determine the response function W_{TT}, for example, one extracts the $\cos 2\phi_l$-amplitude from the measured cross section by weighting each event with $\cos 2\phi_l$. Integration over the full ϕ_l-range of 2π eliminates all terms in Eq. (4) except the one containing W_{TT}. It can easily be seen that the choice of the order of the harmonic function ($n = 1$ or 2) allows one to distinguish between transverse-transverse and longitudinal-transverse response functions. Furthermore, the choice of the harmonic function to be used as a weight (cos or sin) separates $W_{TT}(W_{LT})$ from $W'_{TT}(W'_{LT})$. In order to probe the functions W_T and W_L, one integrates over the angle ϕ_l, which eliminates the contributions from the interference terms W_{TT}, W_{LT}, W'_{TT}, and W'_{LT}. Furthermore, the dependence of the cross section on the leptonic angle θ_l can be used to differentiate between W_T and W_L. Selecting

events with a small angle θ_l reduces the contribution of the longitudinal component, therefore probing the transverse response. The sensitivity to the longitudinal response can be enhanced by selecting large θ_l. As observed from Table I, one can also increase the sensitivity of W_L with respect to W_T by selecting large virtual-photon masses, since $C_T W_T$ is proportional to M_γ^{-2} and $C_L W_L$ is independent of M_γ (k_0 is nearly constant for our kinematics).

III. THEORETICAL MODELS DESCRIBING THE $pp \to ppe^+e^-$ PROCESS

In the previous section we introduced the nuclear current J and coupled it to the leptonic current j which resulted in the decomposition of the cross section into longitudinal and transverse components. In this section we will focus on the current J and present models for the $pp \to ppe^+e^-$ process describing this quantity and the related response functions W_i. Two different approaches have been developed to describe virtual bremsstrahlung in pp scattering: a relativistic low-energy calculation, inspired by the low-energy theorem (LET), and a fully relativistic microscopic model.

A. Low-energy calculation

The LET calculation expresses the bremsstrahlung amplitude in terms of the well-known elastic process, represented by the on-shell T matrix and the static properties of the proton (mass, charge, and magnetic moment). This is achieved by first calculating a so-called external amplitude, from the external current J^{ext} of the leading-order diagrams. Next, the total amplitude is obtained by adding to the external current an internal current $J = J^{\mathrm{ext}} + J^{\mathrm{int}}$. The internal current, J^{int} is constructed by making use of current conservation ($k_\mu J^\mu = 0$), and partially represents higher-order diagrams like meson-exchange and rescattering contributions.

In general, the construction of a LET model is not unique. In Ref. [18] two different LET calculations have been introduced. Both models construct their amplitude using the on-shell T matrix obtained by a one-boson-exchange potential as solution of the Lippman-Schwinger equation. They differ in the expansion method applied to calculate from the on-shell T matrix, the matrix elements needed for the off-shell kinematics associated with the virtual-bremsstrahlung process. Calculations were performed for both approaches. At kinematics close to the elastic proton-proton scattering limit, i.e., small photon energies, the two approaches give identical results, as expected from the nature of a LET expansion. At the kinematics relevant for the present experiment, differences of 30% in the cross section between the two LET calculations are found. In this paper we only show the results of the approach labeled VL (virtual-low) in Refs. [17,18], since it fits our data best.

B. Microscopic model

The basis of this model developed by Martinus et al. [7] is the Bethe-Salpeter (BS) equation. A relativistic one-boson-exchange potential, developed by Fleischer and Tjon [21–23], forms the solution of the BS equation. The result is
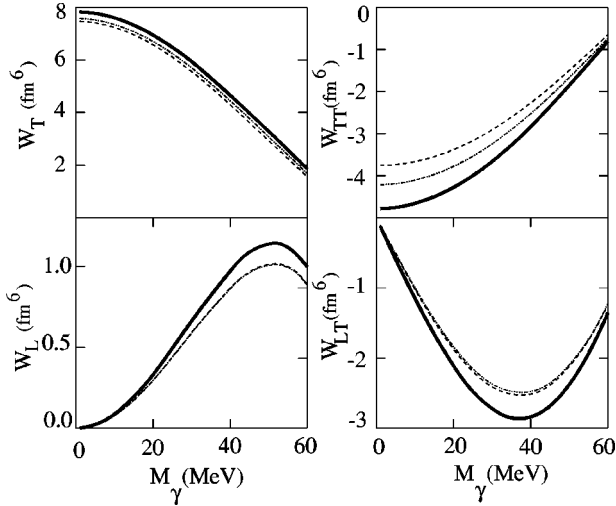
FIG. 3. Predictions of the microscopic model for the response functions W_T, W_L, W_{TT}, and W_{LT} are shown as a function of M_γ, for coplanar kinematics, with $\theta_{p1}=6°$, $\theta_{p2}=15°$, and $\theta_\gamma=140°$. Solid lines include contributions from two-body currents (MEC and Δ) and negative-energy states. Dotted lines do not include negative-energy states. Dashed lines do not include negative-energy states or two-body currents.

a T matrix, which already comprises relativistic and off-shell characteristics of the pp-scattering process. The external and rescattering contributions for bremsstrahlung are obtained by making use of this T matrix. In contrast to the LET calculation, the microscopic model employs the full T matrix. It should be noted that in the on-shell limit, the T matrix of the microscopic model is different from the on-shell T matrix used in the LET calculations. To check the difference between the T matrices, the predictions of the microscopic model and the LET calculations, at kinematics close to the elastic limit were compared. Deviations were found to be less than 10%.

Two-body effects (meson exchange and Δ contributions) are added perturbatively. Also in this respect, the microscopic model differs from the LET calculation. The latter partially takes these higher-order diagrams into account by including an internal current J^{int} and by applying current conservation. Furthermore, negative energy states are calculated explicitly. The contribution of specific diagrams to the different RFs are shown in Fig. 3. Whereas W_{TT} shows equally strong contributions from two-body currents (meson exchange currents and Δ excitations) and negative energy states, the longitudinal RFs (W_L and W_{LT}) are primarily sensitive to the inclusion of negative energy states. Clearly with accurate measurements of all these observables the individual contributions can be tested experimentally.

IV. MONTE CARLO EVENT GENERATOR

With four particles in the exit channel there are twelve observables which in fact are all measured. Energy and momentum conservation reduces the twelve observables to eight. Theory has chosen the parameters of the eightfold differential cross section of Eq. (1). Since we want to compare

with theory, our experimental data have to be brought into the form of Eq. (1) or a lower-order integrated version of it. Limited counting statistics did not allow us to produce an eight-fold differential cross section of the $pp\to ppe^+e^-$ process $(d^8\sigma/d\Omega_{p_1}d\Omega_{p_2}dM_\gamma d\theta_\gamma d\cos\theta_l d\phi_l)$ experimentally. Therefore, the experimental data were integrated over all observables, except the one of interest.

For a comparison with theory, the model calculations have to be integrated over the same phase space as the data. Analytically, this is difficult to perform. First of all, the available calculations produce response functions for a specific kinematics and do not give an analytical expression. Secondly, the boundaries of the experimental setup and the detector acceptances are difficult to express analytically. Finally, as demonstrated by Block [24], the analytical evaluation of the phase space for four or more particles becomes prohibitively complex. Therefore, a Monte Carlo event generator was developed to produce kinematically allowed $pp\to ppe^+e^-$ events.

We employed the N-body phase-space program GENBOD [25]. For each event the corresponding phase-space density is calculated and presented as a weight factor g. Next, the amplitude squared $|A|^2$ is obtained from the model calculation in question (LET or fully relativistic microscopic model), and the total weight of the event is obtained by multiplying $|A|^2$ with g. The product $|A|^2g$ can be used to directly calculate the absolute cross section without the need of further normalization. This has been checked by comparing the result obtained for a small region of phase space given by $\Delta\Omega_{p_1}\Delta\Omega_{p_2}\Delta\theta_\gamma\Delta M_\gamma\Delta\Omega_l$ with an exact calculation.

Finally, the events have to be folded with the experimental filter. To this end we have applied the detector-simulation package GEANT3 [26] to describe the spatial boundaries of the experiment and to realize the electronic thresholds in effect for the energy signals of the detector components.

V. EXPERIMENTAL PROCEDURE

The experiment reported here has been performed at KVI to study bremsstrahlung processes in the pp system using the 190 MeV polarized-proton beam provided by the superconducting cyclotron AGOR. The bremsstrahlung photon can be real or virtual. The present paper discusses the virtual-bremsstrahlung process. Virtual-photon production is detected via the electron-positron pair emitted in $pp\to ppe^+e^-$.

Due to the extremely small reaction cross sections involved, high luminosities together with good detection acceptances are necessary for these measurements. The total cross section for elastic proton-proton scattering is $\approx 10^4$ μb, while the proton-proton real-bremsstrahlung cross section $pp\to pp\gamma$ is of the order of 1 μb. The total cross section of virtual bremsstrahlung is still of order α smaller (≈ 10 nb). The goal of the present bremsstrahlung experiment is to study intermediate states far off the mass shell. This is achieved by measuring two high-energy leptons in coincidence with two protons at small forward angles. The requested kinematics results in a dramatic reduction of the

detector acceptance for bremsstrahlung events. An efficient trigger is needed to reduce the event rate resulting from the dominant elastic channel. In addition, other trigger conditions are concurrently measured (such as scaled-down elastic events, cosmic-ray events, minimum-bias events). These events are used in the off-line analysis to determine detector efficiencies as well as estimating sources of contamination and background. This experiment was performed with an integrated luminosity of 520 pb^{-1}. The product of the total experimental detector acceptance ($\approx 3 \times 10^{-3}$) and efficiency ($\epsilon = 0.361$) was $\approx 1 \times 10^{-4}$. A total of 600 events were identified with the $pp \rightarrow ppe^{+}e^{-}$ process.

A. The liquid-hydrogen target

The very small cross sections required the use of relatively thick liquid hydrogen targets with thin windows in order to minimize background. The target cell [27] used in the experiment is made of aluminum of high purity for optimizing the thermal conductivity and had a minimum amount of material in the median plane. Together with its gas leads, it is mounted on a vertical cryogenic cold head, which can independently cool the target cell down to temperatures as low as 12 K. The operational target pressure and target temperature were chosen to be above 140 mbar and 15 K for hydrogen. The cylindrically shaped target cell was 6 mm thick and 20 mm in diameter. This thickness translates to 42 mg/cm^{2} of hydrogen material in the target. The target was mechanically maintained in a continuous wobbling motion in order to decrease the local heating caused by the energy loss of the beam particles transversing the target. The beam spot at the target was 2 mm in diameter.

To minimize the contribution from the target window relative to the actual target material and to minimize the stopping power of the target, a very thin target window was used. The choice of material for the window was based on the mechanical strength at low temperatures, its resistance to radiation and its quality of not being permeated by LH$_2$. A detailed test and comparison between various materials [27] led to the use of a synthetic aramid foil of 4 μm thickness. The material of the two aramid foils (entrance and exit) corresponds to a combined thickness of 1.2 mg/cm^{2}. When the target is in its operational mode, the bulging of the cell results in an effective liquid-hydrogen thickness of 50 mg/cm^{2}. Together with an averaged beam current of 6 nA an experimental luminosity of 1×10^{33} cm^{-2} s^{-1} is achieved. The luminosity was limited primarily by the maximum tolerable singles count rates for the forward-angle detectors.

B. The small-angle large-acceptance detector

The small-angle large-acceptance detector (SALAD) [11] was used for measuring the two outgoing protons of the $pp \rightarrow ppe^{+}e^{-}$ events. This detector features two multiwire proportional chambers (MWPC) for determining the position of the protons, 24 plastic energy scintillators for measuring their kinetic energy, and 26 plastic veto scintillators placed behind the energy scintillators to reduce the trigger rate of the elastic channel. The total solid angle of the detector is about 400 msr. Protons are detected at polar angles between
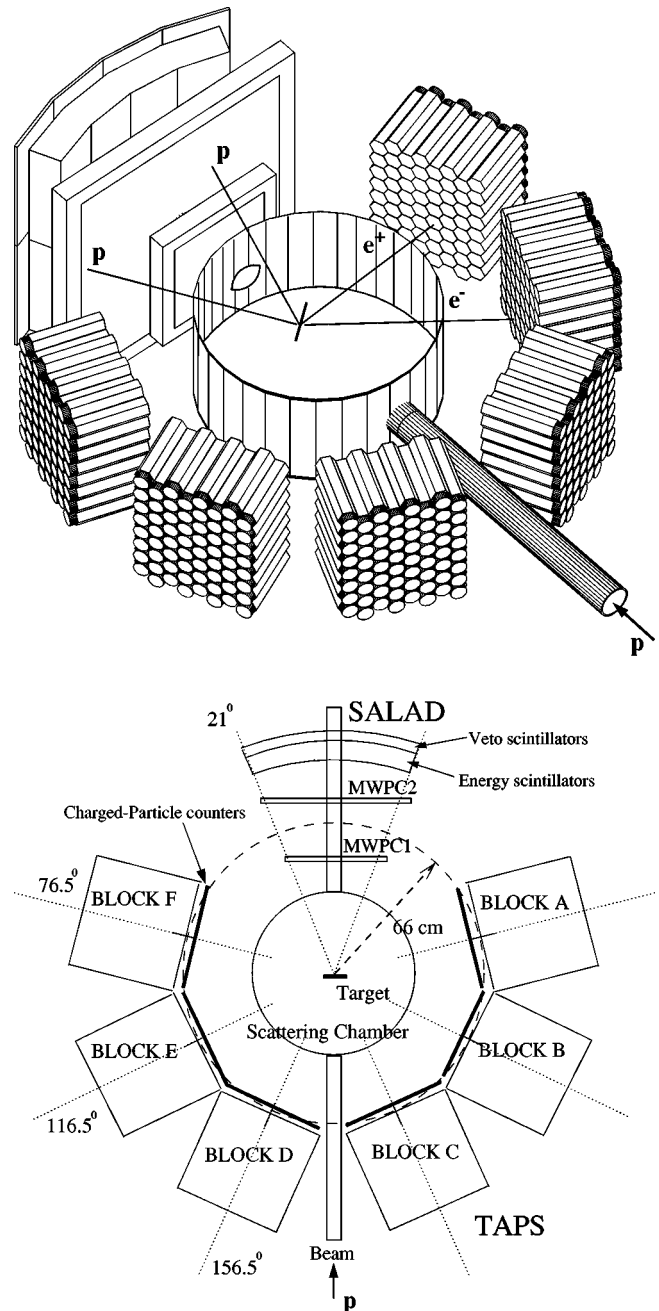

FIG. 4. Schematic drawing giving a perspective view (upper) and a top view (lower) of TAPS and SALAD as used in the present experiment. TAPS used for detecting the $e^{+}e^{-}$ pairs is configured in the block geometry.

6° and 26° with full azimuthal coverage below 21°. A schematic view of the detector is given in Fig. 4.

The first chamber, labeled MWPC1 and with dimensions 380×380 mm^{2}, consists of three wire planes: a plane with wires in the horizontal (x) direction, another in the vertical (y) direction, and a diagonal plane (u), respectively. The u plane is used to overcome ambiguities in multiprong events. The second chamber, labeled MWPC2 with dimensions 840×840 mm^{2}, consists of two planes (x and y). Both MWPCs have a central hole to allow the passage of the beam. The intersection points in the two chambers define the
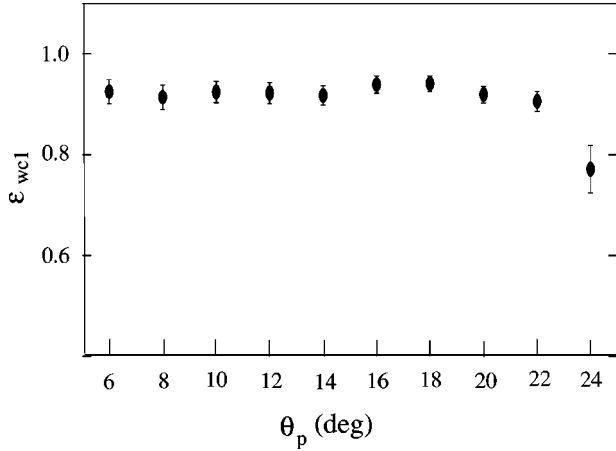
FIG. 5. Efficiency to identify a proton track in the first wire chamber as a function of the scattering angle of the proton θ_p.

FIG. 6. Measured energy distribution of the protons for the $pp \rightarrow ppe^+e^-$ events.

trajectory of the particle. The angular resolution of the chambers is 0.5°. Together with the target spot, the trajectory was extrapolated to indicate the correct scintillator where the energy of the particle should have been measured.

The MWPCs were read out using the commercially available LeCroy PCOS III system. The efficiency maps of the wire chambers were obtained according to the method outlined in Ref. [28], by analyzing elastically scattered protons, which were continuously measured throughout the whole experiment. Given the dominance of the elastic channel this can be achieved within a short measuring period of a few minutes. The efficiency of each chamber is calculated by multiplying the individual plane efficiencies. The efficiency of MWPC1 as a function of the proton scattering angle θ_p is shown in Fig. 5. This efficiency distribution, obtained from an off-line analysis of the present data, corresponds to a total measuring time of 2 h. Averaging both wire-chamber efficiencies, weighted with the accumulated charge measured by a Faraday cup over the full experiment, gives a combined single-proton wire chamber efficiency of $\epsilon_{wc}=0.851 \pm 0.001$. Detection of both protons of the event finally corresponds to an efficiency of ϵ_{wc}^2.

Behind the two wire chambers, 24 plastic scintillators (Bicron BC-408) were placed for measuring the energy of the protons. As shown schematically in Fig. 4, these detectors were arranged as a curved segmented layer of scintillators, consisting of two sections (top and bottom) containing 12 scintillator bars each. Each scintillator bar is trapezoidal in cross section and is pointed towards the target so that a given proton track intersects only one bar. The height (h), width (w), and thickness (d) of these bars are $h=436$ mm, $w=61.2$ mm (front), $w=68.7$ mm (back), and $d=112.5$ mm, respectively. Each bar is coupled via a light guide to a XP2282/B phototube, which is able to operate at high count rates (1 MHz). The scintillators were used to determine the energy of protons with a 10% resolution up to 130 MeV. The effective energy threshold for protons was 20 MeV, caused by energy loss of these particles before reaching the scintillators. Due to hadronic interactions while the protons traverse the scintillator, these detectors are not 100% efficient. ϵ_{had} is the efficiency for detecting the full energy of the
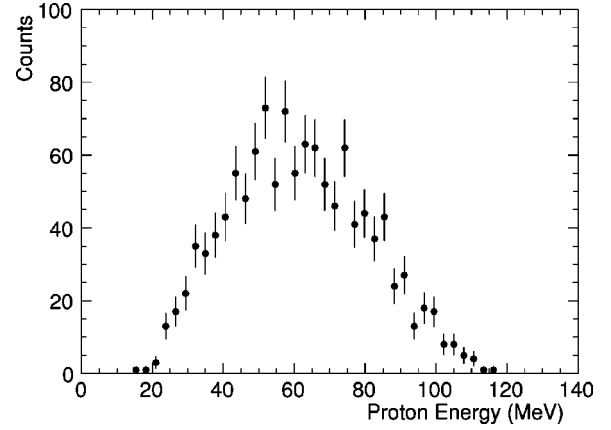
protons in the scintillators. The latter efficiency is obtained by Monte Carlo simulations featuring the simulation package GEANT3 [26] and is found to be on average 0.95 per proton. The actual efficiency correction is done on an event-by-event basis with individual energy-dependent efficiencies for each proton. The proton energy distribution for the $pp \rightarrow ppe^+e^-$ events, as measured in the present experiment, is shown in Fig. 6. Both proton energies are included in this figure resulting in a wide energy distribution.

Protons with energies larger than 130 MeV punch through the 112.5 mm thick scintillator. For 190 MeV protons impinging on a liquid-hydrogen target, protons with energies >130 MeV are associated with the elastic channel. In order to reduce the elastic trigger rate, a segmented layer of 26 plastic veto scintillators (again consisting of a top and bottom section but this time of 13 scintillators each) was placed behind the energy scintillators. Each veto scintillator overlaps partly with two energy detectors. The dimensions of these bars are $h=480$ mm, $w=71.2$ mm (front), $w=71.9$ mm (back), and $d=10$ mm, respectively. The solid angle covered by the veto detectors is larger than the one of the energy detectors in order to account for multiple scattering of protons in the energy scintillators. Elastic scattering events, corresponding to high-energy protons which punch through the thick energy scintillators, are detected by the thin veto scintillators and rejected by the trigger unit. One or more elastically scattered protons coincident in a certain time window with two inelastically scattered protons are not rejected by the trigger. In the off-line analysis, accompanying elastically scattered protons are recognized by analyzing their tracks, as defined by the MWPC detectors, and by the corresponding energy depositions in the thick energy detectors and the thin veto counters.

The luminosity of the experiment of 1×10^{33} cm^{-2} s^{-1}, resulted in a total elastic rate of about 10 MHz in the detection volume. In the experiment, the individual energy-scintillator rates were ≈ 500 kHz, while the veto scintillators were operating at a rate of ≈ 400 kHz.

A dedicated CAMAC trigger module, the SALAD trigger module STM, was developed at KVI to provide a flexible trigger condition for the SALAD detection system. As input, the trigger module receives the constant-fraction discrimi-

nated (CFD) signals from all 50 plastic scintillators and an external strobe to establish a coincidence trigger. A set of internal data registers and memory-lookup units defines four programmable trigger outputs. During the experiment, one output served as main trigger, and the remaining three were used as diagnostic triggers. A detailed description of the trigger module can be found in Ref. [29].

The primary task of the STM was to recognize inelastic proton-proton coincidences by the requirement $N_E - N_V \geqslant 2$, where N_E is the number of signals from the energy scintillators above threshold and N_V the corresponding number from the veto scintillators. With this condition, pp bremsstrahlung events accompanied by elastic events will also be accepted as good candidates. The external strobe was obtained from the leading-edge trigger of TAPS, defining the photon or leptons.

The STM efficiency ϵ_{STM} is determined in the off-line analysis as outlined in Ref. [29]. The efficiency drops from 0.96 for an external strobe rate (TAPS) of 2 kHz to 0.87 for a strobe rate of 20 kHz.

C. The two-arm photon spectrometer

The measurement of the positions and the energies of the electron and positron was done with the two-arm photon spectrometer (TAPS) [12]. This detector consists of 384 hexagonal BaF$_2$ crystals, each with an inscribed diameter of 5.4 cm and 25 cm in length. TAPS has been divided up into six closely packed blocks, each containing 64 crystals. These blocks are placed around the target position in the median plane at polar angles of 76.5°, 116.5°, and 156.5° at a distance of 66 cm from the target (see Fig. 4), resulting in a coverage of the polar angle of the virtual photon between 60° and 180°. In this configuration TAPS provides the possibility to detect e^+e^- pairs with large virtual-photon masses up to the kinematical limit of 93 MeV/c^2.

The full energy of a lepton with a typical energy of 30–50 MeV is determined with a resolution of 3–4 MeV. This is achieved by measuring the complete electromagnetic shower, spread over several BaF$_2$ crystals. The set of adjacent crystals which give a signal above the CFD threshold (± 0.5 MeV) is called a cluster. The direction of the lepton is determined using the information on the position and the energy deposited in each crystal of the cluster. The position of the cluster $\vec{X}$ is given by

$$\vec{X} = \frac{\sum_i E_i \vec{x}_i}{\sum_i E_i}, \tag{5}$$

where member i of the cluster has the position $\vec{x}_i$ and the deposited energy E_i. The geometrical opening angle of a single TAPS crystal, as used in the present experiment, is 5°.

Particle identification is possible by measuring the time of flight, exploiting the excellent timing properties (≈ 700 ps) of BaF$_2$ crystals. Figure 7 demonstrates the possibility to
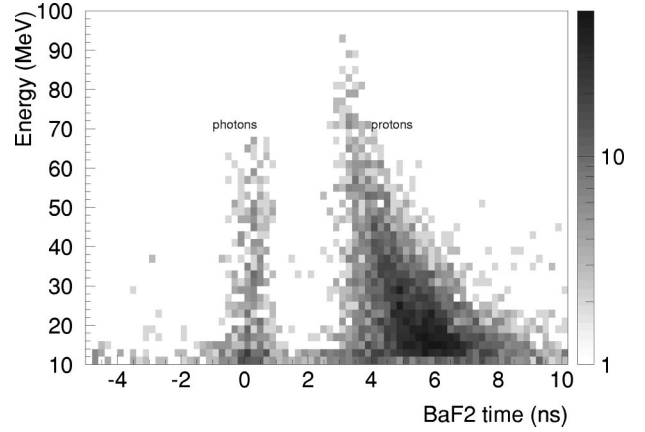

FIG. 7. The time of one of the BaF$_2$ crystals (block F) relative to the cyclotron radio-frequency signal, versus the energy deposition. Photons and electrons and positrons are well separated from the protons.

separate particles traveling with the speed of light (photons, electrons, and positrons) from the heavier protons. Here, the relative time between a signal from one of the CFDs and a signal from the cyclotron RF is plotted and adjusted to $\Delta t = 0$ for photons.

In front of each BaF$_2$ crystal, a charged-particle counter (CPC) was mounted (labeled CPV in Ref. [12]), consisting of a 5 mm thick hexagonal plastic scintillator (NE102A) with an inscribed diameter of 6.5 cm. This detector allows to separate leptons from photons by measuring the energy loss ΔE deposited by the traversing particles. Each CPC scintillator is read out by an individual photomultiplier. The light from the CPC paddles is transported to the photomultiplier banks, above and below the BaF$_2$ blocks, via plexiglass lightguides. Therefore, each lepton traverses at most 15 mm of material before entering the BaF$_2$ crystal. The leading-edge discriminator levels of the CPCs were set individually just above the noise level and below the energy deposition of minimum-ionizing particles (≈ 1 MeV). The ΔE information obtained from the CPCs was essential to identify the $pp \rightarrow ppe^+e^-$ channel against the equally strong $pp \rightarrow pp\gamma\gamma$ reaction.

To determine the efficiency of the CPC detectors, we collected events which obeyed the $pp \rightarrow ppe^+e^-$ selection criteria, as described below, and for which at least one of the clusters in TAPS originated from an incident charged particle, as determined by the appropriate CPC, while no charge condition was requested for the other cluster. The efficiency of the CPC for a single lepton was then calculated as

$$\epsilon_{CPC} = \frac{\text{number of events with both clusters charged}}{\text{total number of preselected events}}. \tag{6}$$

Care was taken that no background events were included in the analysis of determining ϵ_{CPC}. As a precaution, the contamination was minimized by applying a cut on the energy-sharing angle of $\theta_l > 40°$, thereby enhancing the number of events which would make it through all kinematical conditions. We note, however, that the measured θ_l dis-

tribution was found to be in good agreement with the simulated lepton decay kinematics. The efficiency to detect a single lepton was found to be $\epsilon_{CPC} = 0.840 \pm 0.050$ and weakly dependent on energy. The efficiency value was primarily a consequence of the electronic threshold applied to these detectors. The total efficiency for detecting two leptons is given by the square of ϵ_{CPC}, i.e., a value of 0.706 ± 0.059. The CPC efficiencies have been studied for each TAPS block independently and were found to be the same within the uncertainties.

Three leading-edge discriminators (LED), used for trigger purposes, were available: one for the signals from the CPCs and two for the BaF_2 signals. The latter two were set with an energy threshold of approximately 5 MeV, the ''LED low,'' and 15 MeV, the ''LED high,'' respectively. For the $pp \rightarrow ppe^+e^-$ channel the geometrical arrangement of TAPS and SALAD was such that at least one of the leptons had an energy above 15 MeV. Therefore ''LED high'' was used as the main trigger in coincidence with the trigger from the STM for observing the $pp \rightarrow ppe^+e^-$ reaction. Other TAPS discriminator signals, the RF signal of the cyclotron and SALAD CFD signals were downscaled and ORed with the main trigger for diagnostic purposes, for luminosity monitoring and for the determination of individual detector efficiencies.

VI. DATA ANALYSIS

A. Event selection

In the experiment, various triggers were used for specific channel selections. The $pp \rightarrow ppe^+e^-$ events represent only a very small subset of the total amount of data which were stored on tape because the main coincidence trigger was in many cases generated by other reactions. In order to isolate the events which correspond to the $pp \rightarrow ppe^+e^-$ reaction, we exploited the energy, position, and time information from the detectors. In a presort, we selected those events for which two inelastically scattered protons were detected by SALAD. In the analysis we requested at least two wire-chamber tracks plus signals from the corresponding energy scintillators and no energy deposition in the veto scintillators behind them. Furthermore, for each event, TAPS was required to have identified two electromagnetic showers, both with a time of flight consistent with leptons, i.e., around $\Delta t = 0$ (see Fig. 7).

For each event of the presorted data set, the position and energy of all four exit particles (two protons and two leptons) were determined, resulting in 12 observables per event in total. Due to energy and momentum conservation, however, one only needs eight variables in order to define the full kinematics of the process. Exploiting the four extra observables leads to a strong reduction of unwanted background (kinematically uncorrelated events). Here, we have used the following method: first the positions where the final-state particles hit the detectors are determined; secondly from this information we calculate (by applying energy and momentum conservation) the energies of these particles; and finally we compare these ''reconstructed'' energy values with the measured values obtained from TAPS and SALAD. To cal-
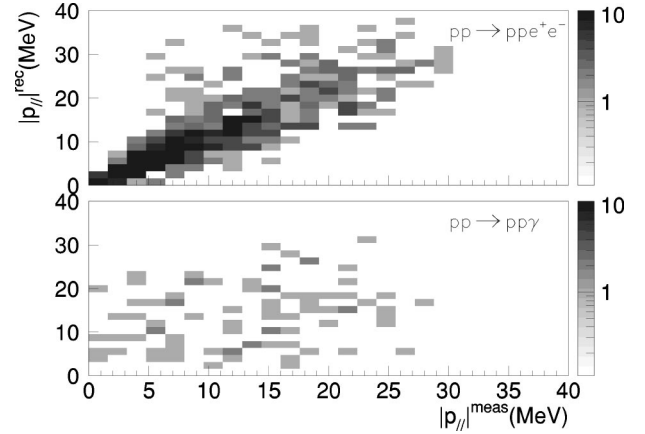

FIG. 8. Measured versus reconstructed momentum of one of the two lepton clusters in TAPS. In the top figure the reconstruction algorithm assumes an event from the $pp \rightarrow ppe^+e^-$ reaction. In the bottom part the reconstruction is performed assuming the cluster to be the result of a $pp \rightarrow pp\gamma$ event with subsequent conversion of the photon into e^+e^-.

culate the energies of the four exit particles from their measured angles, we have resorted to a numerical strategy based on the Newton-Raphson algorithm with a modification to converge from almost any initial guess [30]. The initial guess for the particle momenta is obtained from the experimentally measured energies of the two protons and two leptons. The reconstruction algorithm does not always find a solution. This is primarily due to the experimental uncertainties in the kinematical observables. ϵ_{rec} refers to the efficiency of the kinematical reconstruction algorithm, which was found to be 0.900 ± 0.010.

A further reduction of the data set is performed by applying acceptance windows when comparing the reconstructed momenta with the measured values. The sizes of the windows are based on the detection resolution and have been chosen such that the contribution of the contamination is reduced to a minimum without a significant loss of $pp \rightarrow ppe^+e^-$ candidates. The combined effect of presorting the data and applying kinematical reconstruction cuts is to reduce the original data set by a factor of 10^5, resulting in approximately 20 000 candidates.

So far the information of the CPCs has not been used. Therefore, the reduced data set contains also events from the double-photon process $pp \rightarrow pp\gamma\gamma$. In order to differentiate between the two reactions, one applies the information from the CPCs. We define a charged cluster if one CPC, corresponding to a BaF_2 member of the cluster, was present. For the selection of $pp \rightarrow ppe^+e^-$ events we require two charged clusters. This requirement reduces the number of events by another factor of 10.

The quality of the $pp \rightarrow ppe^+e^-$ events after applying the above mentioned cuts and selecting events for which $M_\gamma > 15$ MeV, is illustrated in Fig. 8. As an example, the component along the beam direction ($p_\parallel$) of the measured momentum of the electromagnetic cluster in TAPS with the smaller energy is compared with the reconstructed $p_\parallel$ momentum. Such a comparison is possible because the event is

overdetermined. Note that no cut has been applied on this observable. In the top part of Fig. 8, we assumed the event to result from a $pp \to ppe^+e^-$ event. A clear correlation is observed, which is well reproduced by Monte Carlo simulations. The few events which fall significantly outside the correlation band are events at the edge of a TAPS block, in which case part of the electromagnetic shower is lost. In the bottom part of the figure, we assumed the event to be resulting from the real-photon production process $pp \to pp\gamma$ with subsequent conversion of the photon into e^+e^-. Most of the events do not survive the kinematical windows used, and of those few which do survive the correlation observed in the top panel of Fig. 8 is lost. Therefore using an additional window on this observable one can reduce further the background.

B. Study of data contamination and sources of background

In the previous section we discussed the constraints which were put on the total data set in order to isolate events from the $pp \to ppe^+e^-$ reaction. In this section we discuss methods to estimate the amount of background left in the selected data set. Different techniques have been applied, depending upon the type of background. We studied the following types of background: accidental background, background originating from real photons and reactions induced in the target foil.

We define accidental background, when a part of the event does not correlate with the rest of the event. For example, three of the four final-state particles result from a given reaction, whereas the fourth particle results from another reaction which took place during the same beam burst. The amount of this type of contamination can be estimated by studying the time differences between the particles, since the probability of a double vertex within the same beam burst is identical to the one in consecutive beam bursts (the cyclotron radio frequency corresponds to a time separation between beam bursts of 17 ns). By using an event-mixing analysis, which allows to increase the amount of accidentals by merging the information of a given event with information from another event, one can generate an unlimited amount of accidental events. Labeling a completely correlated event as $ppee$, the following types of accidental events are generated: $ppex$, $pxee$, $ppxx$, $xxee$, and $pxex$. Here, x indicates the missing information obtained from another uncorrelated event.

These simulated accidental events are subsequently analyzed by using the same cuts as applied to the $pp \to ppe^+e^-$ candidates. The background distributions obtained in this way are normalized to the accidental background of the original (unmixed) data set. The normalization is obtained by inspecting the time spectrum and taking the ratio between prompt coincidence events with those in consecutive beam bursts. Due to the much larger number of generated accidentals, it is now possible to estimate the full background spectra even in phase-space regions of small cross section.

The accidental background has been studied as a function of many observables. In Fig. 9 the most dominant accidental contaminations ($ppex$ and $pxee$) are shown as function of
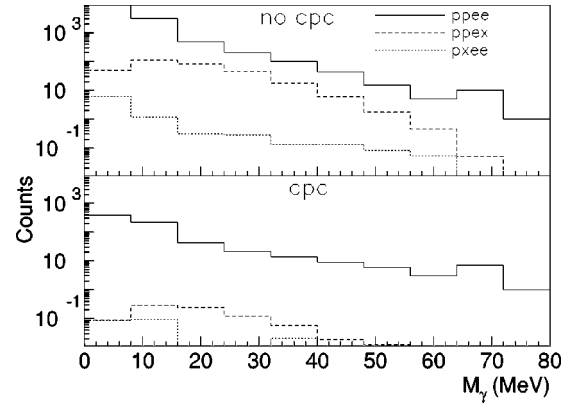

FIG. 9. Accidental contamination of the type $ppex$ and $pxee$ in comparison with unmixed events ($ppee$). The analysis was applied to approximately half of the total data set. In the top panel, the CPCs were not used in the analysis. In the bottom panel, the two clusters in TAPS were required to be charged (CPC signal present).

the virtual-photon mass M_γ. In the top part of the figure, the analysis is shown in case the CPC information has not been used. Note that the contribution from the contamination of the type $ppex$ is significant for $20 < M_\gamma < 60$ MeV. If the CPCs are used in the analysis (only charged clusters are accepted) all types of background reduce to a negligible contribution of less than 2% for the complete virtual-photon mass range. Thus accidental background (including $ppxx$, $pxex$, etc.) can be ignored in the analysis of the $pp \to ppe^+e^-$ reaction.

Another type of contamination results from external pair creation ($\gamma \to e^+e^-$), caused by the material near the target (beam pipe, walls of scattering chamber, vertical cryogenic cold-head, and target cell). A photon initiated from the $pp \to pp\gamma$ process is converted into an electron-positron pair, therefore giving rise to two correlated electromagnetic showers in TAPS together with two correlated inelastic proton tracks in SALAD. This process can be misidentified as a $pp \to ppe^+e^-$ reaction.

To estimate this type of contamination, we made a Monte Carlo study in which the detector-simulation package GEANT3, simulating the complete SALAD-TAPS setup, was combined with an event generator which provides $pp \to pp\gamma$ events according to the LET calculation. The simulated data thus obtained were analyzed in the same way as the actual data from the experiment. This analysis showed that the maximum contribution occurs for $M_\gamma < 10$ MeV where the opening angle between the electron and positron is small. For this virtual-photon mass region it is estimated to be 10%. The contamination resulting from external pair creation decreases rapidly as a function of the virtual-photon mass. At larger masses ($M_\gamma > 15$ MeV) the contamination from external conversion is negligible.

A similar analysis has been performed for the double-photon process, $pp \to pp\gamma\gamma$ in which one of the photons has converted externally into an electron-positron pair. The likelihood of misidentifying such an event as a $pp \to ppe^+e^-$ event, within the kinematical cuts, is extremely small.

TABLE II. Summary of all applied corrections for detector efficiencies, luminosity, and fluctuations in the measured $pp \rightarrow pp\gamma$ cross section.

Wire-chamber efficiency	ϵ_{wc}	0.851 ± 0.001
Reconstruction algorithm	ϵ_{rec}	0.900 ± 0.010
Hadronic interactions	ϵ_{had}	0.950 ± 0.010
SALAD-Trigger Module efficiency	ϵ_{STM}	0.870 ± 0.020
CPC efficiency	ϵ_{CPC}	0.840 ± 0.050
Luminosity correction	η_{lum}	0.812 ± 0.012
$\sigma(pp \rightarrow pp\gamma)$ variations		1.000 ± 0.085

The background resulting from the entrance and exit foils of the target was measured under conditions where the target was emptied of liquid hydrogen. These data were recorded during the experiment for an effective time period of 8 h (compared to 200 h of running with the liquid hydrogen). A quantitative analysis showed that the amount of misidentified events of this kind, satisfying all applied constraints is, for the experimental integrated luminosity, less than one event.

C. Data normalization

From the number of $pp \rightarrow ppe^+e^-$ events, N_{ppee}, the experimental cross section, σ_{exp}, within the accepted phase space covered by TAPS and SALAD is obtained by

$$\sigma_{exp} = \eta_{lum} \frac{N_{ppee}}{C Q_{eff} d \epsilon}, \qquad (7)$$

with $C = 3.76 \times 10^{-3}$ nC^{-1} mg^{-1} cm^2 nb^{-1}, $Q_{eff} = 2.7 \times 10^6$ nC, $d = 42$ mg/cm^2, $\epsilon = 0.361 \pm 0.045$, $\eta_{lum} = 0.812 \pm 0.012$. Here, d corresponds to the nominal target thickness and Q_{eff} to the total collected charge measured by a Faraday cup and corrected for the dead time of the acquisition system. The latter is experimentally determined using the scaler information of the triggers. The value for the total detection efficiency ϵ is obtained by multiplying the individual efficiencies discussed previously: $\epsilon = \epsilon_{rec} \epsilon_{STM} \epsilon_{wc}^2 \epsilon_{CPC}^2 \epsilon_{had}^2$. Note that also the results for the models, simulated using an event generator in combination with the detector-simulation program GEANT3, were corrected using the same values for ϵ_{had}^2 and ϵ_{rec}. Although we give here for simplicity an average value for ϵ_{had}^2, the detector-simulation program calculates on an event-per-event basis separate efficiencies for each proton. Hence, the uncertainties of the latter two efficiencies drop out in the present comparison of theory and experiment. The uncertainties, however, enter in the estimation of the systematic error in the absolute values for the cross sections. A summary of all efficiencies can be found in Table II.

Due to bulging of the target and uncertainties in the measurement of the Faraday cup, deviations from the integrated luminosity ($C d Q_{eff}$) are expected. These are monitored and corrected for by the elastic pp channel which was measured continuously throughout the experimental period. The experimentally determined pp elastic scattering cross sections, corrected for contamination due to the target foil and corrected for wire-chamber efficiencies, are normalized to the world $p+p$ data set [31]. The luminosity correction factor of $\eta_{lum} = 0.812 \pm 0.012$, is dominantly the result of the bulging of the target [27].

As a further check, we have monitored the $pp \rightarrow pp\gamma$ yield to study the stability, in time, of the measurement. For this, we have divided the total data-taking time period into time intervals of ≈ 15 h each, which give accurate measurements for the cross section of the real bremsstrahlung reaction due to its larger yield. For each time interval the total $pp\gamma$ cross section was inferred. The fluctuations in the experimentally determined cross section are in the order of $\pm 8.5\%$ for the complete experimentally covered solid angle. The fluctuations have been added to the systematic uncertainty of the $pp \rightarrow ppe^+e^-$ cross section determination. These fluctuations are partly caused by taking a constant efficiency for the wire chambers and the trigger unit ϵ_{STM} for the complete experiment. Taking into account all the uncertainties on the measured detector efficiencies (see Table II) and the fluctuations in the experimentally determined $pp \rightarrow pp\gamma$ cross section with respect to the elastic channel, for the covered solid angle, we obtain a systematic uncertainty of $\pm 15\%$.

VII. RESULTS AND COMPARISON WITH MODEL CALCULATIONS

After correcting the $pp \rightarrow ppe^+e^-$ data with the detector efficiencies and applying the normalization to the well-known elastic $p+p$ channel, differential cross sections integrated over the covered phase space were determined as outlined above. These cross sections are now compared with the theoretical predictions folded with the detector acceptance.

In Fig. 10 the differential cross section is shown as a function of the virtual-photon mass and the virtual-photon polar angle. Only statistical error bars are depicted. The additional systematic uncertainty is $\pm 15\%$. Furthermore, the energy of the particles is restricted to $E > 5$ MeV for the leptons, $E > 20$ MeV for the protons, and $M_\gamma > 15$ MeV. The same cuts were used in the calculations. The total integrated (measured) cross section amounts to $3.2 \pm 0.1(\text{stat}) \pm 0.5(\text{sys})$ pb.

The virtual-photon mass distribution for two different proton-angle combinations is shown in Fig. 11. In the top panel of Fig. 11, events are selected for which both proton polar angles θ_p are larger than 15°. The bottom panel shows the differential cross section for proton angles smaller than 15°, i.e., large momentum transfer and consequently large photon total energy. In both Figs. 10 and 11 the $pp \rightarrow ppe^+e^-$ data are compared to two calculations. The solid lines refer to the microscopic model by Martinus *et al.* [7], while the dotted curves refer to the LET calculation [17,18].

The state-of-the-art microscopic calculation overestimates the measured differential cross sections as a function of both the virtual-photon mass and its angle. It predicts a total cross section of 5.9 pb. Since the microscopic calculation explicitly takes into account relativistic effects and different sources of non-nucleonic contributions, the observed large discrepancy between the microscopic model and the data is surprising. Part of the discrepancy resides in the fact that the
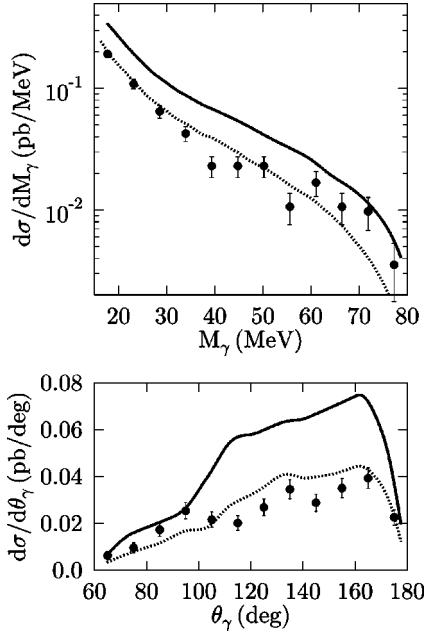
FIG. 10. Top: Differential cross section as a function of the virtual-photon mass (M_γ) of the virtual photon integrated over the full detector acceptance. The bin width in M_γ is 5.5 MeV. Bottom: Virtual-photon angular distribution in the laboratory frame integrated over M_γ from 15 to 80 MeV. The bin width in θ_γ is 10°. Only statistical errors are shown. The solid lines are the result of the microscopic calculation, while the dotted curves refer to the LET calculation.

NN potential of Refs. [21–23] used in the microscopic-model calculation does not provide a good fit to the present-day NN database. At kinematics close to the proton-proton elastic scattering limit, differences of 10% were found between the microscopic predictions and the LET predictions. The latter use an NN potential which fits very well the elastic phase shifts. Note, that the difference between the two calculations becomes larger for protons with polar angles smaller than 15° as shown in Fig. 11, therefore making this part of the phase space ideal for comparing different model predictions with data.

Extraction of the electromagnetic response functions

By exploiting the dependence of the cross section on the lepton angles θ_l and ϕ_l (see Fig. 2), one can experimentally determine the response functions W_T, W_L, W_{TT}, W'_{TT}, W_{LT}, and W'_{LT}. There are two techniques to disentangle the contributions from the various response functions. Using the orthogonality of the harmonic functions [see Eq. (4)], one can isolate all interference terms from the sum of the transverse and longitudinal components, $W_S = W_T + W_L$. The θ_l dependence can then be used to separate W_L and W_T in W_S. In this section we focus on the details of the experimental procedure to extract these response functions. Furthermore, the results are compared to the models previously described.

The limited statistics forced us to integrate the data over the acceptance of the experimental setup. As a result, we define in this section the integral observables $\bar{W}_i$ ($i = T, L$,
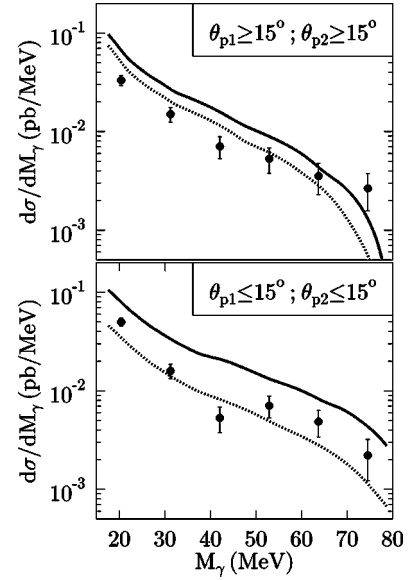

FIG. 11. Differential cross sections as a function of the virtual-photon mass, for protons with polar angles larger than 15° (top panel) and polar angles smaller than 15° (bottom panel). The bin width in M_γ is 11 MeV. Only statistical errors are included. The solid lines show the result of the microscopic calculation and the dotted lines the result of the LET calculation.

TT, LT, TT', LT'), closely related to an average of the response functions W_i as defined in Eq. (4).

We introduce the average of the W_S response $\bar{W}_S = \overline{W_T + W_L}$, and defined it as [see Eqs. (1) and (4)]

$$
\bar{W}_S = \frac{(2\pi)^8 |\vec{p}|}{m_p^3 e^4} \frac{\int_\Omega \left(\frac{d\sigma}{d\Omega}\right)^{\exp} d\Omega}{\int_\Omega R(C_T + C_L) \, d\Omega}
$$

$$
= \frac{1}{\int_\Omega R(C_T + C_L) \, d\Omega} \left\{ \int_\Omega R(C_T W_T + C_L W_L) \, d\Omega \right.
$$

$$
+ \int_\Omega R[C_{TT}(\cos 2\phi_l W_{TT} + \sin 2\phi_l W'_{TT})] \, d\Omega
$$

$$
\left. + \int_\Omega R[C_{LT}(\cos \phi_l W_{LT} + \sin \phi_l W'_{LT})] \, d\Omega \right\}. \quad (8)
$$

In Eq. (8), we integrate over the solid angle, Ω, representing the covered phase space of the setup. Using this definition, it is possible to determine $\bar{W}_S$ unambiguously. The denominator in Eq. (8) is obtained by a Monte Carlo simulation (see Sec. IV) using a model-independent phase-space event generator and the experimental setup simulated with GEANT3. In cases where the leptonic angle, ϕ_l, is fully covered, the interference terms drop out in the integration and Eq. (8) becomes

$$\bar{W}_S = \frac{\int_\Omega R(C_T W_T + C_L W_L) d\Omega}{\int_\Omega R(C_T + C_L) d\Omega}. \tag{9}$$

In order to break down $\bar{W}_S$ into $\bar{W}_T$ and $\bar{W}_L$ one exploits the different dependence of C_L and C_T on θ_l. The contribution from the longitudinal response can be reduced by minimizing C_L. This can be achieved by taking small values for the energy-sharing angle θ_l (see Table I). Within this limit the second term in the denominator on the right-hand side of Eq. (9) becomes small. Hence, the observable $\bar{W}_S$ approximates an average value of W_T over the phase space covered. Conversely, by selecting large values of θ_l to maximize C_L, the observable $\bar{W}_S$ becomes somewhat more sensitive to W_L.

The experimental setup does not fully cover the leptonic angle ϕ_l. Thus $\bar{W}_S$ contains small contributions from the response functions W_{TT}, W_{LT}, W'_{TT}, and W'_{LT}. How well $\bar{W}_S$ represents the averaged transverse response function, W_T, is shown in the left panel of Fig. 12. Here, the experimental results for $\bar{W}_S$ with a cut of $\theta_l < 40°$ (to minimize the contribution from the longitudinal response) are shown and compared with the models. The models, implemented by a Monte Carlo method, are analyzed in the same way as the data and result in the thick solid lines. We have chosen to rescale the W_T component with a factor 0.54. This renormalization, which is only applied to W_T, is an *ad hoc* modification introduced in order to fit the measured virtual-bremsstrahlung cross section (see Figs. 10 and 11). Note that the latter is dominated by the W_T contribution. The contribution of each of the response functions to the total is shown separate. Since some of these contributions are rather small some curves cannot be distinguished from each other in the figures. Both models predict that $\bar{W}_S$ represents quite well the average value for W_T.

By analyzing the data for $\theta_l > 80°$, one hopes to probe experimentally the longitudinal response W_L. In the right panel of Fig. 12 the result for $\theta_l > 80°$ is shown and compared with the simulation obtained using the microscopic model and the LET calculation. The contribution of each response function in the model is depicted. We have chosen to rescale the W_T component of the microscopic model with a factor 0.54, therefore removing the discrepancy observed in Figs. 10 and 11. Clearly, the cut on large energy-sharing angles enhances the sensitivity to the longitudinal response as predicted. At small virtual-photon masses the transverse response function still dominates. That is not surprising since the longitudinal response function W_L vanishes for small virtual-photon masses (see Table I).

Clearly the sensitivity of the data to the longitudinal response is rather poor, which is due to the large experimental uncertainties at large virtual-photon masses. Nevertheless, by looking at the right panel of Fig. 12, one can conclude that after scaling by 0.54 the microscopic model prediction for the longitudinal response function is not in disagreement with the data.
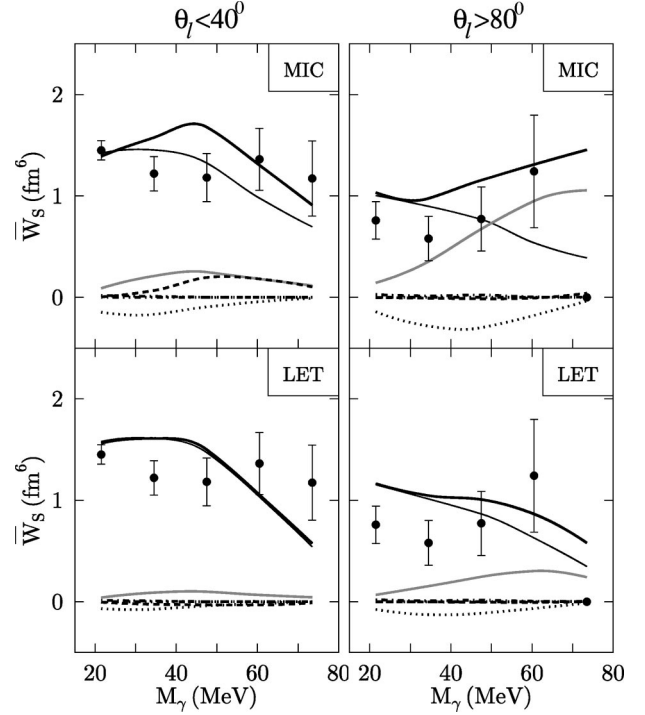

FIG. 12. The experimentally determined average response function, $\bar{W}_S$, is compared with the LET calculation (bottom panel) and the microscopic model (top panel). In the left panel data are shown for which a cut of $\theta_l < 40°$ is made to minimize the contribution from the longitudinal response. In the right panel data are shown for which a cut of $\theta_l > 80°$ is applied in order to enhance the sensitivity to the longitudinal response. The bin width in M_γ is 13 MeV. The solid thick line represents the prediction of the models. The remaining lines are the contributions of the different components: W_T (thin), W_L (gray), W_{TT} (dotted), W_{LT} (dashed), W'_{TT} (dot-dashed), and W'_{LT} (dot-dot-dashed). The transverse response function of the microscopic model for both plots in the top panel has been multiplied by 0.54.

To extract experimentally the interference response functions, we define a more general expression for the averaged response function $\bar{W}_i$ with $i = TT, LT, TT', LT'$ by

$$\bar{W}_i = \frac{\int_\Omega (d\sigma/d\Omega)^{\exp} g_i \, d\Omega}{C \int_\Omega R C_i \hat{g}_i^2 \, d\Omega}, \tag{10}$$

where the functions g_i and $\hat{g}_i$ are given in Table III. As an illustration, we assume that ϕ_l is covered completely, and demonstrate the relation between $\bar{W}_{TT}$ and W_{TT}. In that case, the components T, L, LT, TT', LT' vanish in the integral over $d\Omega_l$, due to the orthogonality of the functions g_i and $\hat{g}_i$ (see Table III). Hence, the averaged transverse-transverse response function, $\bar{W}_{TT}$, results in ($\hat{g}_{TT} = g_{TT}$)

TABLE III. The definitions of the functions g_i and $\hat{g}_i$ used in Eq. (10). For the TT' and LT' components, a special sign-function (either $+1$ or -1) related to the azimuthal angles of the protons is applied to g_i. Here, the index 1 refers to the proton on the side of the photon.

g_T	1	$\hat{g}_T$	1
g_L	1	$\hat{g}_L$	1
g_{TT}	$\cos 2\phi_l$	$\hat{g}_{TT}$	$\cos 2\phi_l$
g_{LT}	$\cos \phi_l$	$\hat{g}_{LT}$	$\cos \phi_l$
$g_{TT'}$	$\frac{1}{2}\sin 2\phi_l \, \mathrm{sgn}[\sin 2(\phi_1-\phi_2)]$	$\hat{g}_{TT'}$	$\sin 2\phi_l$
$g_{LT'}$	$\frac{1}{2}\sin \phi_l \, \mathrm{sgn}[\sin 2(\phi_1-\phi_2)]$	$\hat{g}_{LT'}$	$\sin \phi_l$

$$\bar{W}_{TT} = \frac{\int_\Omega R W_{TT} C_{TT} g_{TT} \, d\Omega}{\int_\Omega R C_{TT} g_{TT}^2 \, d\Omega}. \tag{11}$$

It can easily be shown that also the other averaged interference response functions (W_{LT}, W'_{TT}, and W'_{LT}) behave similarly in case ϕ_l is completely covered experimentally.

The weight functions g_i (and $\hat{g}_i$) are chosen in order to exploit fully the dependence of the cross section on the angle ϕ_l, given in Table I, which is purely determined by QED. For TT' and LT' an additional term is introduced. This was found necessary, since the response functions W'_{TT} and W'_{LT} change sign under the reflection, $Y \rightarrow -Y$. Omitting this additional function would result in an average value of zero for W'_{TT} and W'_{LT}.

Since the dilepton angle ϕ_l is not completely covered experimentally, the averaged interference response functions, $\bar{W}_i$, become a mixture of all the response functions W_i. This can be seen from the results shown in Fig. 13. Here, the deduced response functions are shown together with the predictions of two models shown as the solid line: LET (right panel), and microscopic model (left panel). The remaining lines are the various nonvanishing components W_{TT} (dotted), W_{LT} (dashed), W'_{TT} (dot-dashed), W'_{LT} (dot-dot-dashed). In this plot, the data points shown are obtained by explicitly subtracting the contribution, $\bar{W}_T$, resulting from the transverse response W_T, as predicted by each of the two models.

For the left panels, the renormalized W_T predictions were used for the subtraction. Note that the data points are only weakly dependent upon the model used for the subtraction procedure. The error bars shown contain the contribution of the statistical significance of the data as well as the influence of the systematic error (of 15%) in determining the contribution of W_T which is subtracted from the data. The experimental results for W_{TT}, W_{LT}, W'_{TT}, and W'_{LT} are compared with the corresponding predictions.

Whereas for W_T the microscopic model overestimates the data for all virtual-photon masses, the interference responses are better described. At small virtual-photon masses the microscopic model and the LET calculation are able to predict the data reasonably well within statistics. The microscopic
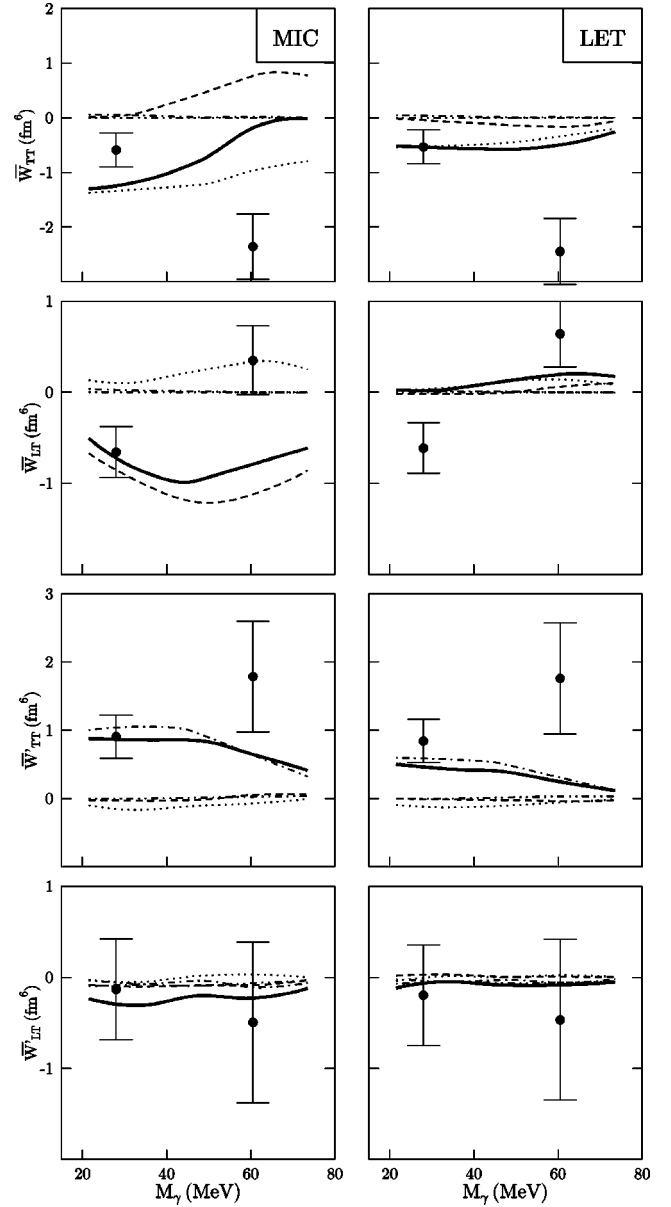

FIG. 13. The deduced interference response functions ($\bar{W}_{TT}$, $\bar{W}_{LT}$, $\bar{W}'_{TT}$, $\bar{W}'_{LT}$) are compared with the results of the microscopic model (left panel) and the LET calculation (right panel). The contribution from W_T has been subtracted using the respective model predictions. The bin width in M_γ is 25 and 40 MeV for the two data points, respectively. The curves are defined in the caption of Fig. 12.

model prediction for the data point corresponding to the lower virtual-photon mass bin is in good agreement with the data for $\bar{W}_{LT}$ and $\bar{W}'_{TT}$, although it clearly underestimates the $\bar{W}_{TT}$ response. The latter is probably related to the observed overestimation of the $\bar{W}_T$ response, as can be expected by the correlation between the definition of these response functions (see Table I).

At large virtual-photon masses, however, discrepancies between both models and the data can be observed, especially in the interference terms $\bar{W}_{TT}$ and $\bar{W}'_{TT}$. Also for $\bar{W}_{LT}$

the microscopic-model prediction disagrees with the data at large M_γ. Clearly, improvements in the theoretical description of the nucleonic currents are needed.

VIII. SUMMARY AND CONCLUSIONS

The well-known coupling of the photon with the nucleon together with the fact that photons (or any electromagnetic probe) interact only relatively weakly with nucleons, make bremsstrahlung production an ideal tool to study details of the nucleon-nucleon interaction. In the present paper dilepton production (e^+e^-) in proton-proton scattering $pp \rightarrow ppe^+e^-$ has been discussed. This process provides new information on the nucleon-nucleon interaction in addition to that obtained by studying the real-photon channel $pp \rightarrow pp\gamma$. However, the relatively small cross section of the $pp \rightarrow ppe^+e^-$ reaction (approximately a factor 1/137 smaller than the cross section of the $pp \rightarrow pp\gamma$ reaction) makes virtual bremsstrahlung difficult to observe. The results shown now clearly demonstrate that these experiments have become feasible.

For the first time, the $pp \rightarrow ppe^+e^-$ channel is measured below the pion-production threshold. The background originating from accidental contamination, from $pp \rightarrow pp\gamma$ events, and from the double-photon process ($pp \rightarrow pp\gamma\gamma$) has been reduced to a negligible level by making use of the good time resolution of the BaF_2 crystals, by applying the information from the charged-particle counters of TAPS, and by exploiting the overdetermined kinematics of the event provided by SALAD. A total of ≈ 600 background-free $pp \rightarrow ppe^+e^-$ events have been extracted from the data. The limited energy resolution of the setup is compensated by the fact that each event is kinematically overdetermined, allowing to reconstruct the energies from the measured position information. The remaining events from the complete data set (originating mainly from $pp \rightarrow pp$, $pp \rightarrow pp\gamma$, and cosmic rays) have been used to calibrate the detectors, to determine individual detector efficiencies, and to obtain the experimental luminosity.

Exclusive differential cross sections have been measured. The total cross section integrated over virtual-photon masses of 15 to 80 MeV/c^2 amounts to 3.2 ± 0.1(stat) ± 0.5(sys) pb. The data are compared to a LET calculation [17,18] and a fully relativistic microscopic model [7], which predict, for the actual detector acceptance, a virtual-bremsstrahlung cross section of 3.4 and 5.9 pb, respectively. Over the entire experimentally covered phase space, the LET calculation gives a better description of the data than the microscopic model. The latter takes explicitly into account the off-shell dynamics of the intermediate protons and the rescattering contributions. Furthermore, the model adds perturbatively contributions from meson-exchange currents and the virtual Δ isobar. Similar comparisons were made for the real-photon bremsstrahlung data [6]. There, the higher statistics obtained allowed the comparison in very small regions of the phase space. It is noted that the microscopic model also overestimates the real-photon data.

The data have also demonstrated that the leptonic-angle dependence of the cross section can be exploited to probe specific directional components of the nucleon current. The cross section can be decomposed into six independent observables, the electromagnetic response functions W_i. The most dominant contribution, the transverse response function W_T, can be determined with relatively good accuracy. Extracting the remaining response functions (longitudinal, transverse-transverse, and longitudinal-transverse response functions) is difficult and requires, apart from good statistics, a complete coverage of the leptonic angles θ_l and ϕ_l. Due to the limited coverage of the leptonic angles in the present work, the experimental decomposition of these response functions has a large contribution from the dominant transverse response function (W_T). This contribution has been subtracted using the model predictions, making the experimentally obtained result somewhat model dependent.

We have compared the extracted values of the interference terms with the predictions of the LET calculation and the microscopic model. For the latter calculation, we have adjusted the predicted W_T response function by multiplying it with a normalization factor of 0.54 to account for the discrepancy between data and calculation in the total cross section. Within this normalization and within the statistical accuracy of our data both models show significant deviations from the data. For low M_γ (15–40 MeV), the microscopic model predicts all but the $\bar{W}_{TT}$ response. The underestimation of the latter is most likely correlated with the overestimation of the $\bar{W}_T$ response. For large M_γ (40–80 MeV) both models show significant deviations from the data. Clearly, improvements in the theoretical description of the nucleonic currents are needed.

APPENDIX

In this appendix it is explained how to obtain the square of the reaction amplitude for the $pp \rightarrow ppe^+e^-$ process in terms of the transverse (W_T), longitudinal (W_L), transverse-transverse (W_{TT}, W'_{TT}), and longitudinal-transverse (W_{LT}, W'_{LT}) response functions. The coupling of the leptonic transition current, j_μ, with the nucleonic transition current J_μ is described by QED and results in a squared amplitude given by [32]

$$|A|^2 = -\frac{e^4}{2m_l^2 M_\gamma^4}[|J\cdot l|^2 + M_\gamma^2(J\cdot J^*)]. \tag{A1}$$

We are interested in the decomposition of the spatial components of the current density $\vec{J}$ into a longitudinal ($\vec{J}_L$) and a transverse ($\vec{J}_T$) part

$$\vec{J} = \vec{J}_L + \vec{J}_T, \tag{A2}$$

where we define $\vec{J}_L$ to be the component in the direction of the virtual-photon momentum $\vec{k}$, defined by the z axis with unit vector $\vec{e}_z$:

$$\vec{J}_L = \frac{\vec{J}\cdot\vec{k}}{|\vec{k}|^2}\vec{k} \equiv J_L\vec{e}_z. \tag{A3}$$

We decompose the transverse component into two components, from coupling a photon with positive helicity $+1$, J_{+1}, and a photon with negative helicity $-1, J_{-1}$:

$$\vec{J}_T = J_{+1}\vec{e}_{+1}^* + J_{-1}\vec{e}_{-1}^*, \tag{A4}$$

with unit vectors $\vec{e}_{\pm 1} = \mp\sqrt{\frac{1}{2}}(\vec{e}_x \pm i\vec{e}_y)$. The y axis is chosen along $\vec{k}\times\vec{p}$ with $\vec{p}$ denoting the incoming proton momentum (see Fig. 2).

The terms $J\cdot J^*$ and $J\cdot l$ are evaluated as

$$J\cdot J^* = J_0 J_0^* - \vec{J}\cdot\vec{J}^*$$

$$= \frac{|\vec{k}|^2}{k_0^2}|J_L|^2 - |J_L|^2 - |J_T|^2$$

$$= -\frac{M_\gamma^2}{k_0^2}|J_L|^2 - |J_T|^2 \tag{A5}$$

and

$$J_\mu l^\mu = J_0 l_0 - \vec{J}\cdot\vec{l}$$

$$= \frac{|\vec{k}|^2|\vec{l}|\cos\theta_l}{k_0^2}J_L - |\vec{l}|\cos\theta_l J_L$$

$$- \sqrt{\frac{1}{2}}[J_{-1}(\vec{e}_x + i\vec{e}_y) - J_{+1}(\vec{e}_x - i\vec{e}_y)]\cdot\vec{l}$$

$$= -\frac{M_\gamma^2}{k_0^2}|\vec{l}|\cos\theta_l J_L - \sqrt{\frac{1}{2}}|\vec{l}|\sin\theta_l[J_{+1}e^{-i\phi_l}$$

$$- J_{-1}e^{i\phi_l}], \tag{A6}$$

where θ_l and ϕ_l are the polar and azimuthal angles of $\vec{l}$, respectively (see Fig. 2). Equations (A5) and (A6) are obtained by substituting the components J_0 and l_0, using the relations $k_\mu J^\mu = 0$ and $k_\mu l^\mu = 0$, with

$$J_0 = \frac{|\vec{k}|J_L}{k_0}, \tag{A7}$$

$$l_0 = \frac{|\vec{k}||\vec{l}|\cos\theta_l}{k_0}. \tag{A8}$$

The next step is to evaluate $|J\cdot l|^2$ as given in Eq. (A1). One obtains

$$|J\cdot l|^2 = \frac{M_\gamma^4}{k_0^4}|\vec{l}|^2\cos^2\theta_l|J_L|^2 + \frac{1}{2}|\vec{l}|^2\sin^2\theta_l|J_T|^2$$

$$- \frac{1}{2}|\vec{l}|^2\sin^2\theta_l(2\,\mathrm{Re}(J_{+1}J_{-1}^*)\cos 2\phi_l)$$

$$- \frac{1}{2}|\vec{l}|^2\sin^2\theta_l(i(J_{-1}J_{+1}^* - J_{+1}J_{-1}^*)\sin 2\phi_l)$$

$$+ \frac{M_\gamma^2|\vec{l}|^2}{2\sqrt{2}k_0^2}\sin 2\theta_l(2\,\mathrm{Re}(J_L J_{+1}^* - J_L J_{-1}^*)\cos\phi_l)$$

$$+ \frac{M_\gamma^2|\vec{l}|^2}{2\sqrt{2}k_0^2}\sin 2\theta_l[i(J_L J_{+1}^* - J_{+1}J_L^*$$

$$+ J_L J_{-1}^* - J_{-1}J_L^*)\sin\phi_l]. \tag{A9}$$

Substitution of Eqs. (A9) and (A5) into Eq. (A1) together with a transformation to spatial components

$$J_L = J_z,$$

$$J_{+1} = -\sqrt{\frac{1}{2}}(J_x + iJ_y),$$

$$J_{-1} = \sqrt{\frac{1}{2}}(J_x - iJ_y), \tag{A10}$$

results in

$$|A|^2 = \frac{e^4}{2m_l^2 M_\gamma^2}\Bigg[\left(1 - \frac{|\vec{l}|^2}{2M_\gamma^2}\sin^2\theta_l\right)(|J_x|^2 + |J_y|^2)$$

$$+ \left(1 - \frac{|\vec{l}|^2}{k_0^2}\cos^2\theta_l\right)\left(\frac{M_\gamma^2}{k_0^2}|J_z|^2\right)$$

$$+ \left(\frac{|\vec{l}|^2}{2M_\gamma^2}\sin^2\theta_l\cos 2\phi_l\right)(|J_y|^2 - |J_x|^2)$$

$$+ \left(\frac{|\vec{l}|^2}{2M_\gamma^2}\sin^2\theta_l\sin 2\phi_l\right)[-2\,\mathrm{Re}(J_x J_y^*)]$$

$$+ \left(\frac{|\vec{l}|^2}{2k_0 M_\gamma}\sin 2\theta_l\cos\phi_l\right)\left(-2\frac{M_\gamma}{k_0}\mathrm{Re}(J_z J_x^*)\right)$$

$$+ \left(\frac{|\vec{l}|^2}{2k_0 M_\gamma}\sin 2\theta_l\sin\phi_l\right)\left(-2\frac{M_\gamma}{k_0}\mathrm{Re}(J_z J_y^*)\right)\Bigg]. \tag{A11}$$

The response functions W_T, W_L, W_{TT}, W'_{TT}, W_{LT}, and W'_{LT} are defined by the factors containing the nucleonic currents in the equation above.

[1] J.R. Bergervoet *et al.*, Phys. Rev. C **41**, 1435 (1990).

[2] V.G.J. Stoks *et al.*, Phys. Rev. C **48**, 792 (1993); **49**, 2950 (1994).

[3] R. Machleidt, F. Sammarucca, and Y. Song, Phys. Rev. C **53**, R1483 (1996).

[4] K. Michaelian *et al.*, Phys. Rev. D **41**, 2689 (1990).

[5] B. von Przewoski *et al.*, Phys. Rev. C **45**, 2001 (1992).

[6] H. Huisman *et al.*, Phys. Rev. Lett. **83**, 4017 (1999).

[7] G.H. Martinus, Ph.D. thesis, University of Groningen (1998).

[8] H.Z. Huang *et al.*, Phys. Lett. B **297**, 233 (1992).

[9] H.Z. Huang *et al.*, Phys. Rev. C **49**, 314 (1994).

[10] A. Yegneswaran *et al.*, Nucl. Instrum. Methods Phys. Res. A **290**, 61 (1990).

[11] N. Kalantar-Nayestanaki *et al.*, Nucl. Instrum. Methods Phys. Res. A (to be published).

[12] A.R. Gabler *et al.*, Nucl. Instrum. Methods Phys. Res. A **346**, 168 (1994).

[13] J.G. Messchendorp *et al.*, Nucl. Phys. **A641**, 618c (1998).

[14] J.G. Messchendorp *et al.*, Phys. Rev. Lett. **82**, 2649 (1999).

[15] J.G. Messchendorp *et al.*, Few-Body Syst., Suppl. **10**, 355 (1999).

[16] J.G. Messchendorp *et al.*, Phys. Rev. Lett. **83**, 2530 (1999).

[17] A.Yu. Korchin and O. Scholten, Nucl. Phys. **A581**, 493 (1995).

[18] A.Yu. Korchin, O. Scholten, and D. van Neck, Nucl. Phys. **A602**, 423 (1996).

[19] C. Ciofi degli Atti, Prog. Part. Nucl. Phys. **3**, 163 (1980).

[20] S. Frullani and J. Mougey, Adv. Nucl. Phys. **14**, 1 (1984).

[21] J. Fleischer and J. Tjon, Nucl. Phys. **B84**, 375 (1974).

[22] J. Fleischer and J. Tjon, Phys. Rev. D **15**, 2537 (1977).

[23] J. Fleischer and J. Tjon, Phys. Rev. D **21**, 87 (1980).

[24] M. Block, Phys. Rev. **101**, 796 (1959).

[25] F. James, ''Monte Carlo phase space,'' Lectures given in the Academic Training Programme of CERN, CERN 68-15 (1968).

[26] R. Brun, F. Bruyant, A.C. McPherson, and P. Zanarini, GEANT3 Users Guide, Data Handling Division DD/EE/84-1, CERN (1986).

[27] N. Kalantar-Nayestanaki, J. Mulder, and J. Zijlstra, Nucl. Instrum. Methods Phys. Res. A **417**, 215 (1998).

[28] M. Volkerts *et al.*, Nucl. Instrum. Methods Phys. Res. A **428**, 432 (1999).

[29] S. Schadmand *et al.*, Nucl. Instrum. Methods Phys. Res. A **423**, 174 (1999).

[30] W.H. Press, S.A. Teukolsky, W.T. Vettering, and B.P. Flannery, *Numerical Recipes in C* (Cambridge University, Cambridge, 1992).

[31] R.A. Arndt *et al.*, Phys. Rev. C **56**, 3005 (1997).

[32] D. Van Neck *et al.*, Nucl. Phys. **A574**, 643 (1994).